RSC Advances

PAPER

View Article Online
View Journal | View Issue

Cite this: *RSC Adv.*, 2021, **11**, 37504

H_2O_2-independent chemodynamic therapy initiated from magnetic iron carbide nanoparticle-assisted artemisinin synergy†

Fan Zhao,‡[ab] Jing Yu,‡*[ab] Weiliang Gao,[ab] Xue Yang,[c] Liying Liang,[ab] Xiaolian Sun,[d] Dan Su,[e] Yao Ying,[ab] Wangchang Li,[ab] Juan Li,[ab] Jingwu Zheng,[ab] Liang Qiao,[ab] Wei Cai,[ab] Shenglei Che*[ab] and Xiaozhou Mou*[c]

Chemodynamic therapy (CDT) is a booming technology that utilizes Fenton reagents to kill tumor cells by transforming intracellular H_2O_2 into reactive oxygen species (ROS), but insufficient endogenous H_2O_2 makes it difficult to attain satisfactory antitumor results. In this article, a H_2O_2-free CDT technique with tumor-specificity is developed by using pH-sensitive magnetic iron carbide nanoparticles (PEG/Fe_2C@Fe_3O_4 NPs) to trigger artemisinin (ART) to *in situ* form ROS. ART-loaded PEG/Fe_2C@Fe_3O_4 NPs are fabricated for the enormous release of Fe^{2+} ions induced by the acidic conditions of the tumor microenvironment after magnetic-assisted tumor enrichment, which results in the rapid degradation of the PEG/Fe_2C@Fe_3O_4 NPs and release of ART once endocytosed into tumor cells. *In situ* catalysis reaction between the co-released Fe^{2+} ions and ART generates toxic ROS and then induces apoptosis of tumor cells. Both *in vitro* and *in vivo* experiments demonstrate that the efficient Fe-enhanced and tumor-specific CDT efficacy for effective tumor inhibition based on ROS generation. This work provides a new direction to improve CDT efficacy based on H_2O_2-independent ROS generation.

Received 28th June 2021
Accepted 19th October 2021

DOI: 10.1039/d1ra04975e

rsc.li/rsc-advances

Introduction

Chemodynamic therapy (CDT), that employs highly cytotoxic reactive oxygen species (ROS) generated from endogenous hydrogen peroxide (H_2O_2) *via* the Fenton-type reactions to induce tumor cell apoptosis, has been intensively investigated for tumor therapy nowadays.[1,2] Benefiting from the over-produced endogenous H_2O_2 which is the characteristic feature of the tumor microenvironment (TME), CDT has been recognized as an emerging therapeutic strategy with high therapeutic specificity and low invasiveness.[3,4] However, the concentration of intratumoral H_2O_2 (50–100 μM), although at a higher level compared with normal cells, is still insufficient to maximize the Fenton catalytic efficacy, which restricts the clinical application of CDT.[5–7] To address this limitation, substantial efforts have been devoted to increasing the level of intratumoral H_2O_2, such as applying natural enzymes like glucose oxidase (GOx), nicotinamide adenine dinucleotide phosphate oxidase (NOX), and superoxide dismutase (SOD) as H_2O_2 self-supplying systems to *in situ* generate H_2O_2 inside tumor.[8–10] Nevertheless, the rigorous reaction condition further confines the therapeutic efficiency of CDT utilizing these strategies. Recently, Wang and coauthors applied ferrous ion (Fe^{2+}) to catalyze linoleic acid hydroperoxide (LAOOH) to produce abundant ROS through the Russell mechanism, overcoming the dependence on H_2O_2 concentration by CDT.[11] This suggests a potential alternative to H_2O_2-dependent CDT.

Artemisinin (ART), a class of sesquiterpene lactone extracted from *Artemisia annua*, has been broadly used to treat malaria.[12,13] Over the last 10 years, studies have suggested that ART containing endoperoxide bridge also has a therapeutic effect on various tumor cells.[14,15] The critical mechanism for antitumor ability of ART is that peroxide bridge structure (R–OO–R′) inside of ART could be catalysis-cleaved by Fe^{2+} within tumor cells to produce toxic carbon-centered free radicals (a kind of ROS).[16–19] Thus, a H_2O_2-independent CDT agent can be constructed based on ART. Noteworthy that Fe^{2+} plays an irreplaceable role in tumor cell killing for ART-based drugs and sufficient Fe^{2+} may make a remarkable contribution to maximize the therapy efficiency of ART.[20–24] Whereas, the concentration of Fe^{2+} at the tumor site is generally much lower than the

[a]*College of Materials Science and Engineering, Zhejiang University of Technology, Hangzhou 310014, China. E-mail: yujing@zjut.edu.cn; cheshenglei@zjut.edu.cn*

[b]*Research Center of Magnetic and Electronic Materials, Zhejiang University of Technology, Hangzhou 310014, China*

[c]*Clinical Research Institute, Zhejiang Provincial People's Hospital, Hangzhou 310014, China. E-mail: mouxz@zju.edu.cn*

[d]*Key Laboratory of Drug Quality Control and Pharmacovigilance (China Pharmaceutical University), Ministry of Education, Nanjing 210009, China*

[e]*Department of Oncology, Zhejiang Provincial People's Hospital, Hangzhou 310014, China*

† Electronic supplementary information (ESI) available: Figures and discussions. See DOI: 10.1039/d1ra04975e

‡ These authors contributed equally to this manuscript.

optimum concentration of Fe^{2+} which can exhaust the anti-tumor ability of ART, leading to an unsatisfactory therapeutic efficiency.[25] Therefore, designing a nanocarrier for co-delivery of ART and Fe^{2+} to tumor cells can be an ideal strategy for the enhancement of CDT that independent from endogenous H_2O_2.

Iron carbide nanoparticles (ICNPs), a kind of nano-intermetallic iron-based compounds, have gained enormous attention for their extraordinary magnetic property which renders them to be T_2 contrast agents in magnetic resonance imaging (MRI).[26–29] Besides, ICNPs with appropriate surface modification could be excellent drug carriers, and the high saturation magnetization of ICNPs endows them magnetic targeting property.[30–32] Interestingly, our previous works suggested that ICNPs in which the valence state of iron tends to be zero valence can easily release Fe^{2+} under acidic condition and chronically remain stable in the neutral environment.[33] Consequently, taking advantage of their pH-sensitivity, ICNPs can be designed as 'iron storage pool' to specifically release Fe^{2+} at acidic microenvironment of the tumor to trigger ART.

Herein, core–shell structured ICNPs ($Fe_2C@Fe_3O_4$ nanoparticles), which were capable of pH-triggered Fe^{2+}-release, were designed as the nanocarriers for ART. Benefiting from the high saturation magnetization, an enrichment of $Fe_2C@Fe_3O_4$ NPs together with ART in tumor sites was feasible by magnetic targeting. Combined with the acidic microenvironment of tumor, the designed $Fe_2C@Fe_3O_4$ nanocarrier was able to resolve at tumor, release both Fe^{2+} and ART synchronously for yielding quantity of toxic ROS *in situ* to damage proteins and nucleic acid, and consequently induce cell death which significantly enhance the CDT efficiency (Scheme 1). This study paves a new direction to improve CDT efficacy based on H_2O_2-free ROS generation.

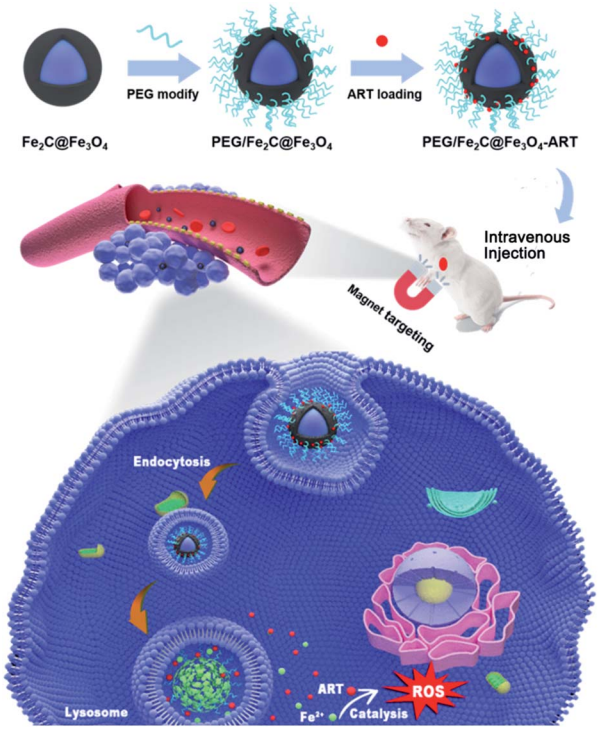

Scheme 1 Schematic illustration of ART loaded PEG/$Fe_2C@Fe_3O_4$ NPs to tumor cells assisted by an externally applied magnetic field and the antitumor mechanism of the ART delivery system.

Results and discussion

$Fe_2C@Fe_3O_4$ NPs were synthesized by a two-step synthetic method.[34] Based on transmission electron microscopy (TEM) image (Fig. 1a), the as-synthesized NPs showed monodisperse core–shell structure with uniform size at approximately 18 nm, which was consistent with the data of dynamic light scattering (DLS) (Fig. S1†). The core size of $Fe_2C@Fe_3O_4$ NPs was measured to be 14 ± 2 nm, while the shell thickness was approximately 1 ± 0.5 nm. The crystallization of the NPs could be identified in the high-resolution transmission electron microscopy (HRTEM) image (Fig. 1b). The lattice spacing in the core was 0.206 nm, corresponding to the (101) plane of highly crystallized Fe_2C, while the shell structure showed an amorphous feature of Fe_3O_4.[34] The crystal structure of the NPs was further determined by X-ray diffraction (XRD) (Fig. 1c). All the diffraction peaks could be well-indexed to the Fe_2C core (JCPDS no. 37-0999), while no obvious peak of Fe_3O_4 was observed, due to its low crystallization. To verify the composition of the $Fe_2C@Fe_3O_4$ NPs, X-ray photoelectron spectroscopy (XPS) was applied, and the result indicated the coexistence of carbon, oxygen, and iron (Fig. 1d). The energy-dispersive spectroscopy (EDS) further confirmed that obtained $Fe_2C@Fe_3O_4$ NPs were composed of Fe, C, and O elements (Fig. S2†). Besides, the magnetic property of $Fe_2C@Fe_3O_4$ NPs was tested by using a vibrating sample magnetometer (VSM) at room temperature. The saturation magnetization (M_s) value of $Fe_2C@Fe_3O_4$ NPs was 65.483 emu

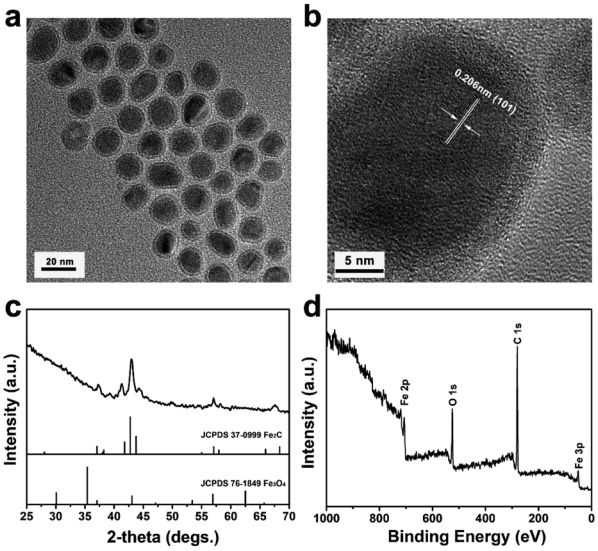

Fig. 1 Characterization of $Fe_2C@Fe_3O_4$ NPs. (a) TEM image of $Fe_2C@Fe_3O_4$ NPs. (b) HRTEM image of $Fe_2C@Fe_3O_4$ NPs. (c) XRD pattern of $Fe_2C@Fe_3O_4$ NPs (JCPDS no. 37-0999, 76-1849). (d) XPS survey spectrum of $Fe_2C@Fe_3O_4$ NPs.

g^{-1} (Fig. S3†), suggesting their potential as T_2 contrast agents as well as nanocarriers with magnetic targeting.

To endow a hydrophilic nature as well as a long-circulation property to $Fe_2C@Fe_3O_4$ NPs, DSPE-PEG was applied to form PEG/$Fe_2C@Fe_3O_4$ NPs. The data of FT-IR and macrophotograph showed the successful modification of PEG on $Fe_2C@Fe_3O_4$ NPs (Fig. S4 and S5†). TEM image of PEG/$Fe_2C@Fe_3O_4$ NPs obtained from their aqueous dispersions, indicating that there was no obvious morphology change after the ligand addition process (Fig. S6†). In addition, hydrodynamic diameter of PEG/$Fe_2C@Fe_3O_4$ NPs was increased to 96.1 nm and zeta potential was measured to be −21.5 mV (Fig. S7†), which was suitable for enhanced permeability and retention (EPR) effect to achieve practical applications. Furthermore, $Fe_2C@Fe_3O_4$ NPs after PEGylation could keep long-term stability in the aqueous phase (Fig. S8†).

The antitumor activity of ART was related to the concentration of Fe^{2+}. Hence, Fe^{2+} release characteristic of PEG/$Fe_2C@Fe_3O_4$ NPs was firstly explored. Three solutions with pH value of 7.4, 6.5, and 5.4 were applied that corresponding to the environment of normal tissue, tumor site, and lysosomes. As shown in Fig. 2a, the degradation of PEG/$Fe_2C@Fe_3O_4$ NPs in different solutions severed an obvious pH-sensitivity. Iron ions released in pH 5.4 solution increased significantly in the first 4 h, with the amount reached to 63.42% after 24 h, while only 14.02% and 22.04% of iron ions could be released under pH 7.4 and 6.5, respectively. TEM images of PEG/$Fe_2C@Fe_3O_4$ NPs after being dispersed in pH 5.4 and 7.4 media for 24 h, further confirming that the NPs could be degraded only in pH 5.4 solution (Fig. 2b and c). In addition, strong hypo-intensities in T_2-weighted magnetic resonance imaging (T_2-MRI) of PEG/$Fe_2C@Fe_3O_4$ NPs, which induced from their high magnetization, was reduced by altering the incubation solution from physiological condition (pH 7.4) to acidic solution (pH 5.4), with the transverse relaxivity (r_2) decreased from 205.11 mM^{-1} s^{-1} to 58.29 mM^{-1} s^{-1} (Fig. 2d). This result further proved the dissolution of the NPs in acidic environment. Color of the solution turned to bright yellow at pH of 5.4, and after adding potassium ferricyanide (a Fe^{2+} indicator), the color became blue, suggesting an efficient release of Fe^{2+} at acidic environment (Fig. S9†). The excellent pH-sensitive Fe^{2+} release ability of PEG/$Fe_2C@Fe_3O_4$ NPs was attributed to successful introduction of amorphous Fe_3O_4 shells which performed stronger pH sensitivity after amorphization.[33,35,36] The above results demonstrated that PEG/$Fe_2C@Fe_3O_4$ NPs were good Fe^{2+} donors in low pH environment.

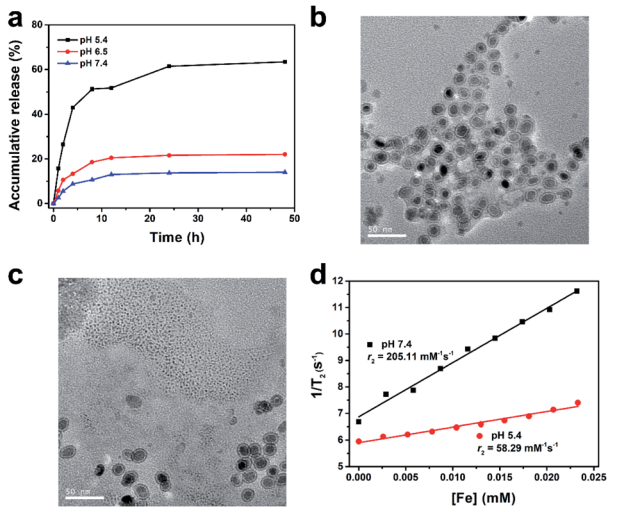

Fig. 2 (a) Accumulative iron ions release of PEG/$Fe_2C@Fe_3O_4$ NPs in PBS with pH 7.4, 6.5 and 5.4. (b) TEM image of PEG/$Fe_2C@Fe_3O_4$ NPs by dispersing in pH 7.4 solution for 24 h. (c) TEM image of PEG/$Fe_2C@Fe_3O_4$ NPs by dispersing in pH 5.4 solution for 24 h. (d) The longitudinal relaxation rates of PEG/$Fe_2C@Fe_3O_4$ NPs dispersing at pH 5.4 or pH 7.4 environment.

PEG was modified onto hydrophobic $Fe_2C@Fe_3O_4$ NPs through ligand addition method, endowing the interspace for loading ART by hydrophobic–hydrophobic interaction. The appearance of the characteristic peaks at the wavelength of 1737 cm^{-1}, between 800 cm^{-1} and 1200 cm^{-1} confirming the loading of ART onto PEG/$Fe_2C@Fe_3O_4$ NPs, which were ascribed to the C–O stretching vibrations, and the O–O and C–O modes of O–O–C (peroxide), respectively (Fig. S10†).[37] The ART loading efficiency was calculated to be 21.9 wt% by using ultraviolet and visible (UV-vis) spectra. Result from TEM image showed the ART loaded PEG/$Fe_2C@Fe_3O_4$ (PEG/$Fe_2C@Fe_3O_4$-ART) NPs could still keep their morphology with good dispersity in aqueous solution (Fig. S11†).

The result from EPR spectrometry showed ART was able to generate carbon-centered free radicals (a kind of ROS) in Fe^{2+}-riched environment (Fig. S12†).[21,23] Considering the acidic environment of lysosome and the efficient release of Fe^{2+} under low pH solution, locating PEG/$Fe_2C@Fe_3O_4$ NPs as an ART activator in lysosomes after being cellular uptake was important. After labelling PEG/$Fe_2C@Fe_3O_4$ NPs with fluorescein isothiocyanate (FITC), cellular uptake assay was carried out by staining nuclei with 4,6-diamidino-2-phenylindole (DAPI) and lysosomes with Lyso-Tracker red. As shown Fig. 3a, green fluorescence from the FITC-labeled NPs was well overlapped with the red fluorescence of Lyso-Tracker, indicating that PEG/$Fe_2C@Fe_3O_4$ NPs were internalized and located in the acidic lysosomal compartment, and should produce ROS consequently.

To verify the capability of PEG/$Fe_2C@Fe_3O_4$-ART NPs in generating ROS in tumor cells, 2,7-dichlorofluorescein diacetate (DCFH-DA), a fluorescent ROS-detection probe was used. Fluorescence emitted from PEG/$Fe_2C@Fe_3O_4$-ART NPs increased with the incubation time, and the fluorescence intensity after 9 h of incubation was 1.8 and 3.6-fold higher compared to the ART alone and PEG/$Fe_2C@Fe_3O_4$ NPs treated group respectively (Fig. 3b). Similarly, observed under a confocal laser scanning microscope (CLSM), a bright green fluorescence could be clearly observed in cells incubated with PEG/$Fe_2C@Fe_3O_4$-ART NPs within 4 h, while in contrast, fluorescence from the cells incubated with ART alone or PEG/$Fe_2C@Fe_3O_4$ NPs was much weaker (Fig. 3c). These results demonstrated that intracellular PEG/$Fe_2C@Fe_3O_4$-ART NPs could boost the generation of ROS *in situ* for tumor therapy.

Cell growth inhibition was then evaluated through MTT assay. As shown in Fig. 3d and S13,† ART alone and PEG/

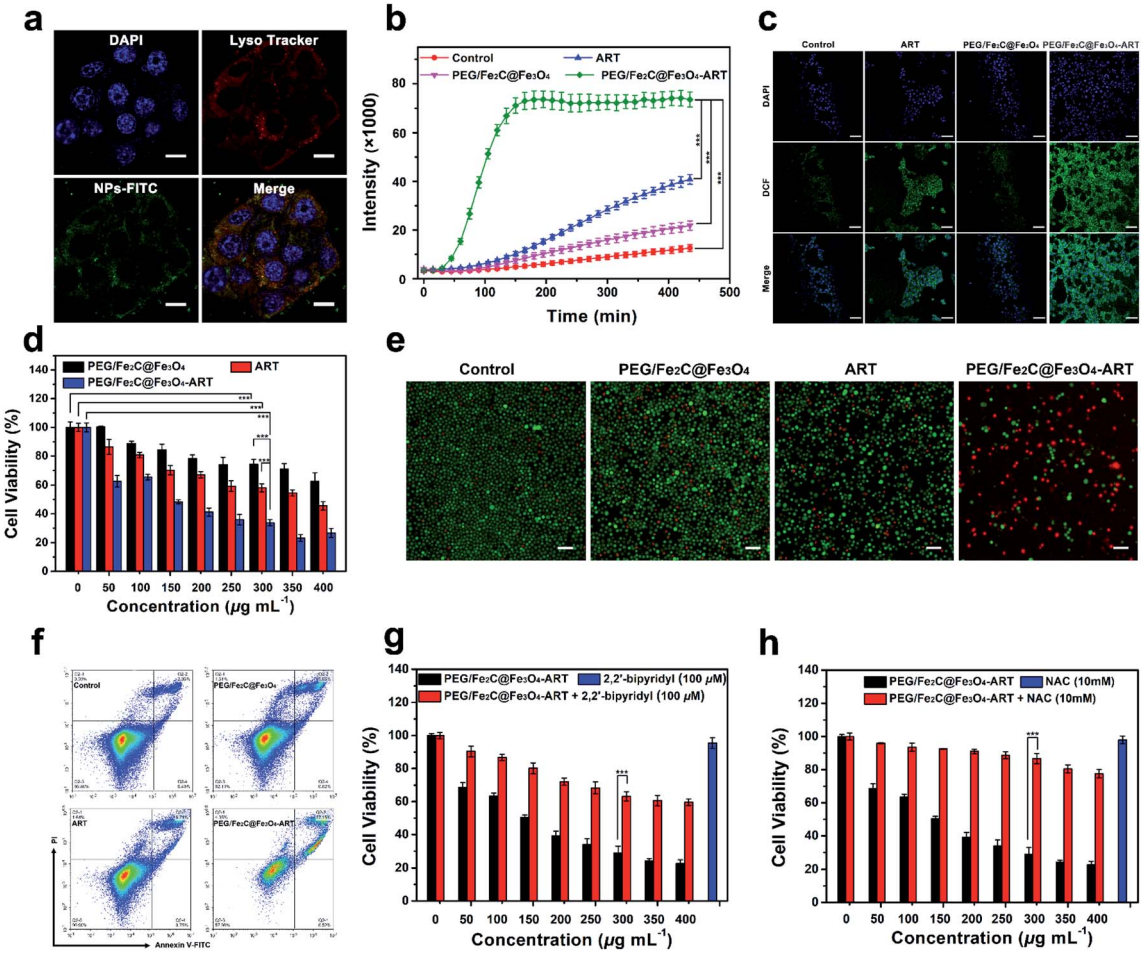

Fig. 3 *In vitro* experiments with PEG/$Fe_2C@Fe_3O_4$-ART NPs. (a) Fluorescence images of 4T1 cells treated with PEG/$Fe_2C@Fe_3O_4$-FITC NPs for 4 h. Nuclei of live cells were stained with DAPI and lysosomes were stained with Lyso-Tracker red (scale bar 15 μm). (b) Time-dependent fluorescent intensity from DCFH-DA labeled 4T1 cells by ART, PEG/$Fe_2C@Fe_3O_4$ and PEG/$Fe_2C@Fe_3O_4$-ART ($n = 3$, mean ± s.d., ***$p < 0.001$). (c) Fluorescence images of DCFH-DA labeled 4T1 cells treated by ART, PEG/$Fe_2C@Fe_3O_4$ and PEG/$Fe_2C@Fe_3O_4$-ART (scale bar 75 μm). (d) Viability of 4T1 cells after different treatments under various conditions for 24 h ($n = 6$, mean ± s.d., ***$p < 0.001$). (e) Fluorescence images of calcein AM (green, live cells) and PI (red, dead cells) costained 4T1 cells after incubation with ART, PEG/$Fe_2C@Fe_3O_4$ NPs or PEG/$Fe_2C@Fe_3O_4$-ART for 24 h. The scale bar represents 100 μm. (f) Flow cytometry analysis in 4T1 cells treated with ART, PEG/$Fe_2C@Fe_3O_4$ NPs or PEG/$Fe_2C@Fe_3O_4$-ART for 24 h. (g) Viability of 4T1 cells incubated with PEG/$Fe_2C@Fe_3O_4$-ART alone or PEG/$Fe_2C@Fe_3O_4$-ART plus 2,2-bipyridyl (100 μM) for 24 h ($n = 6$, mean ± s.d., ***$p < 0.001$). (h) Viability of 4T1 cells incubated with PEG/$Fe_2C@Fe_3O_4$-ART alone or PEG/$Fe_2C@Fe_3O_4$-ART plus NAC (10 mM) for 24 h ($n = 6$, mean ± s.d., ***$p < 0.001$).

$Fe_2C@Fe_3O_4$ NPs were not obviously toxic to 4T1, MDA-MB-231, and HeLa cells. Whereas, the cytotoxicity of PEG/$Fe_2C@Fe_3O_4$-ART NPs was significantly enhanced, demonstrating $Fe_2C@Fe_3O_4$ NPs could improve the antitumor efficiency of ART. Results from live/dead cell staining assay further confirmed this conclusion. By staining live cells with calcein-AM and dead cells with propidium iodide (PI), red fluorescence from PEG/$Fe_2C@Fe_3O_4$-ART NPs 24 h-treated 4T1 cells indicated the induction of cell death (Fig. 3e). It has been reported that cell killing through ROS-mediated pathway could mainly induce cell apoptosis. Flow cytometry was further applied to identify the type of cell death by using the Annexin V-FITC/PI apoptosis detection kit. Obviously, the PEG/$Fe_2C@Fe_3O_4$-ART-treated groups had higher ratios of apoptotic tumor cells compared with other groups (Fig. 3f).

From the phenomenon above, the reason for the enhanced apoptosis of PEG/$Fe_2C@Fe_3O_4$-ART NPs could be ascribed to the efficient *in situ* generation of ROS by released Fe^{2+} and ART. Consequently, Fe^{2+} is sufficient for ART-based tumor therapy. Therefore, 2,2-bipyridyl, a widely used Fe^{2+} chelator was applied to confirm the dependance of Fe^{2+} in the cell killing.[38] Cells incubated with PEG/$Fe_2C@Fe_3O_4$-ART in the presence of 2,2-bipyridyl showed suppressed intracellular ROS production (Fig. S14†), and as a result, significantly increased the cell viability compared with that without 2,2-bipyridyl (Fig. 3g). It proved the involvement of the released Fe^{2+} in the cytotoxicity of PEG/$Fe_2C@Fe_3O_4$-ART NPs. To verify the significance of ROS, *N*-acetyl-cysteine (NAC),[39,40] a ROS scavenger, was applied. As shown in Fig. 3h, the addition of NAC significantly reversed the cytotoxicity induced by PEG/$Fe_2C@Fe_3O_4$-ART NPs, further

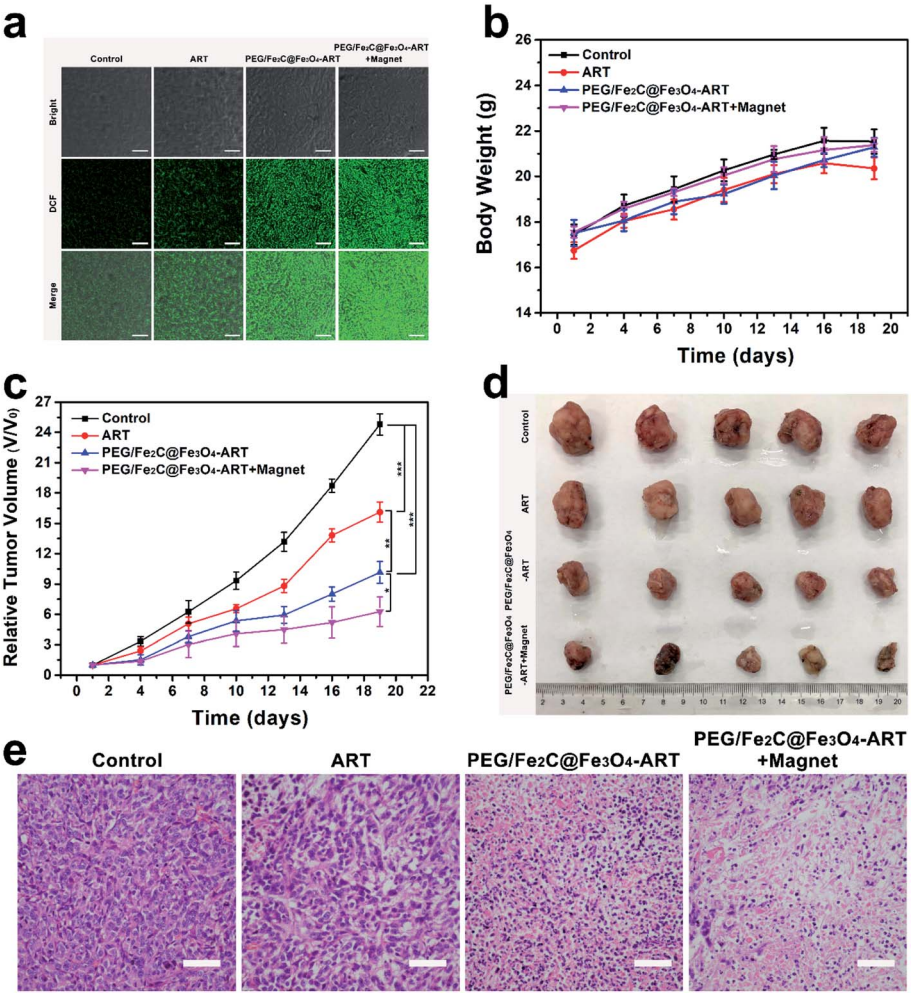

Fig. 4 *In vivo* experiments with PEG/Fe_2C@Fe_3O_4-ART NPs. (a) Fluorescence image of DCFH-DA labeled tumor slices of the mice after the different treatment (scale bar 25 μm). (b) Time course change in the body weight after different treatments ($n = 5$, mean ± s.d.). (c) Time course change in the relative tumor volume after different treatments ($n = 5$, mean ± s.d., $*p < 0.05$, $**p < 0.01$, $***p < 0.001$). (d) Digital photograph of excised tumors after 18 days of various treatments. (e) H&E staining of 4T1 tumor sections in different groups (scale bar 100 μm).

confirmed the cell apoptosis was primarily origined from ROS. From the above, we can conclude that PEG/Fe_2C@Fe_3O_4 NPs can provide Fe^{2+} in tumor cells and *in situ* activate ART to generate abundant ROS, which result in the cytotoxicity for cell killing.

Inspired by the excellent *in vitro* cell growth inhibition based on PEG/Fe_2C@Fe_3O_4-ART NPs, *in vivo* biological performances were then evaluated on 4T1 tumor-bearing mice. Benefiting from the magnetic property of PEG/Fe_2C@Fe_3O_4 NPs, biodistribution of NPs was initially evaluated by measuring Fe concentration in major organs and tumors 24 h post-injection. Compared with magnetic field-free group, in which PEG/Fe_2C@Fe_3O_4 NPs were primarily distributed in liver, and a few NPs accumulated in tumor tissue *via* EPR effect, the magnetic targeting group could effectively accumulate NPs in tumor tissue by locating a magnant at tumor (Fig. S15†). Furthermore, *in vivo* NIR images further verified PEG/Fe_2C@Fe_3O_4 NPs could be effectively accumulated in tumor site by magnetic targeting (Fig. S16†). Together with the acid environment of tumor, the effective enrichment of NPs in tumors by magnetic targeting makes PEG/Fe_2C@Fe_3O_4 NPs as good carriers to effective deliver ART and donate Fe^{2+} for the *in situ* activation of ART by ROS generation.

Thus, we next investigated the *in vivo* tumor ROS concentration. As shown in Fig. 4a, bright green fluorescence was emitted only in the group that had been subjected to magnetic-assisted intravenous (*i.v.*) injection of PEG/Fe_2C@Fe_3O_4-ART NPs after staining with DCFH-DA, illustrating amounts of ROS could be generated by specifically accumulating PEG/Fe_2C@Fe_3O_4-ART NPs in tumor with Fe^{2+}-ART catalysis. The high ROS intensity led to tumor cell apoptosis and even necrosis. Therefore, tumor inhibition assay was then carried out. 4T1 tumor-bearing female Balb/c mice were established and divided into four groups, which were *i.v.* injected with either saline, ART only, PEG/Fe_2C@Fe_3O_4-ART NPs or PEG/Fe_2C@Fe_3O_4-ART NPs with magnetic targeting. Tumor volume and body weight were monitored one-day post-injection. No obvious body-weight changes were observed during the overall therapeutic process

(Fig. 4b). More importantly, tumor growth in the group treated with magnetic-assisted *i.v.* injection of PEG/Fe_2C@Fe_3O_4-ART NPs was significantly suppressed (Fig. 4c and d), compared to the control group, the ART-only group, and *i.v.* injection of PEG/Fe_2C@Fe_3O_4-ART NPs group (Fig. S17†). Besides, tumor sections from mice dissected at the end of the treatment period conducted hematoxylin–eosin (H&E) and TdT-mediated dUTP nick-end labeling (TUNEL) staining, which showed that the multitude of cell necrosis and apoptosis occurred in the tumor sections from mice treated with PEG/Fe_2C@Fe_3O_4-ART NPs (Fig. 4e and S18†). By contrast, no obvious cell necrosis was observed in the control group or the ART-only group, indicating the improved chemotherapeutic efficacy of PEG/Fe_2C@Fe_3O_4-ART NPs for ART-based chemotherapy.

Eventually, systemic biotoxicity valuation is crucial for nanomaterials to clinical research. To explore long-term biosafety, the normal hematology parameters and standard blood biochemical indexes were also measured in healthy mice. As shown in the blood biochemistry and hematology analysis, no obvious changes were induced by PEG/Fe_2C@Fe_3O_4-ART NPs (Fig. S19†). H&E staining also showed no obvious pathological toxicity in the major organs, indicating high biocompatibility of PEG/Fe_2C@Fe_3O_4-ART NPs (Fig. S20†).

Conclusions

In summary, a H_2O_2-free and tumor-selective chemodynamic therapy agent was constructed by ART loaded magnetic iron carbide NP, which *in situ* generated ROS by releasing Fe^{2+} and ART under tumor specificity environment after magnetic targeting. The core–shell structured PEG/Fe_2C@Fe_3O_4 magnetic nanoparticles were synthesized to deliver ART into the tumors, where they could rapidly co-release Fe^{2+} and ART in a tumor-specific manner. The released ART molecules then transformed into toxic ROS by *in situ* catalysis of Fe^{2+}, resulting in apoptosis of tumor cells. These features synchronously endow the nanocarrier with enhanced efficacy and biosafety for tumor-specific therapy. Both *in vitro* and *in vivo* experiments confirmed the high chemotherapeutic efficacy and revealed the related therapeutic mechanism. This work sets an example of iron-based magnetic nanocarrier with excellent Fe^{2+} and drug release behavior in the tumor microenvironment after magnetic-assisted tumor enrichment for *in situ* enhanced Fe^{2+}-dependent chemodynamic.

Experimental section

Materials

Iron carbonyl ($Fe(CO)_5$, 99%), oleylamine (OAm), oleic acid (OAc, 90%), 1-octadecene (ODE, 90%) and ammonium bromide (NH_4Br, 99%) were purchased from Alfa Aesar. Hexane (C_6H_{14}), and ethanol (C_2H_6OH) of analytic grade were from the Juhua Group Factory, China. Artemisinin (ART, 98%) was purchased from J&K. 1,2-Distearoyl-*sn-glycero*-3-phosphoethanolamine-2000 (DSPE-PEG) was purchased from Toyongbio corporation, china. All chemicals were used as received without further purification.

Characterization

X-ray diffraction (XRD) patterns were recorded on a X'Pert PRO X-ray diffractometer equipped with Cu Kα (λ = 1.54178 Å) radiation. Transmission electron microscopy (TEM) was carried out on a FEI Tecnai G2 F30 microscope. High-resolution TEM (HRTEM) was carried out on a FEI Tecnai G2 F30 microscope. Dynamic light scattering was measured using a particle size analyzer (ZetaPALS, Brookhaven Instruments). X-ray photoelectron spectroscopy (XPS) measurements were carried out on an Axis Ultra imaging photoelectron spectrometer (Kratos Analytical Ltd). Magnetization was measured by a superconducting quantum interference device (SQUID). The concentrations of Fe were quantified using an inductively coupled plasma-atomic emission spectrometer (ICP-AES, Profile, Leeman, USA). Fourier transform infrared radiation (FT-IR) spectrum was determined using a Nicolet 6700 spectrometer. Ultraviolet visible (UV-vis) absorption spectra were measured on a HACH DR6000 ultraviolet visible absorption spectrometer.

Synthesis of Fe_2C@Fe_3O_4 NPs

In the typical synthesis, bcc-Fe NPs were firstly synthesized by the following steps. ODE (15 mL), NH_4Br (0.05–0.1 mmol) and OAm (0.4 mL) were mixed magnetically and degassed under a gentle Ar flow for 1 h in a four-neck flask. The solution was then heated to 100 °C and kept at this temperature for 1 h before it was heated further to 180 °C. After that, $Fe(CO)_5$ (0.5–0.7 mL) was injected to the reaction mixture and kept there for 30 min. OAc (0.1 mL) was added *via* a syringe and the resultant solution was aged at 140 °C for another 30 min before it was cooled down to room temperature. The complex was collected through magnetic separation and rinsed three times with ethanol. After centrifugation (5 min, 10 000 rpm), the product was collected and re-dispersed in hexane. ODE (3.0 g), OAm (10 mL) was magnetically blended in the four-neck flask and degassed under a gentle Ar flow for 1 h at 120 °C. Then, the resulted bcc-Fe NPs (5 mmol, in 10 mL hexane) was added *via* a syringe and the reaction solution was heated at 280–340 °C for 15–45 min. The black-brown colored solution was cooled down to room temperature. Ethanol was added and the mixture was centrifuged (5 min, 10 000 rpm) three times. The precipitates were re-dispersed in hexane.

Preparation of ART-loaded Fe_2C@Fe_3O_4 NPs

Fe_2C@Fe_3O_4 (5 mg) was added to chloroform (10 mL) and then sonicated at room temperature. Then artemisinin (10 mg) and DSPE-PEG (20 mg) dissolving in 10 mL chloroform was slowly added to the above Fe_2C@Fe_3O_4 chloroform mixture solution and sonicated for 30 min before the solvent was evaporated by a rotary evaporator. The final products were washed with ethanol to remove the free drug. The loading efficiency of ART was measured by a UV-vis spectrophotometer. Unloaded ART in the supernatant was converted into a UV-absorbing compound through treatment with sodium hydroxide aqueous solution at 50 °C for 30 min and the detection wavelength was 292 nm.

Fe^{2+} release from PEG/$Fe_2C@Fe_3O_4$ NPs

PEG/$Fe_2C@Fe_3O_4$ NPs solution (1 mL) with Fe concentration of 2 mg mL^{-1} was sealed in a dialysis bag (MCWO: 1000 Da), and immersed in 20 mL buffer media (PBS) at different pH values (7.4, 6.5 and 5.4) in a centrifuge tube. Centrifuge tubes were then shaken with a speed of 200 rpm at 37 °C. At given intervals, 1 mL of buffer was collected and analyzed the Fe concentration by ICP-AES. 1 mL fresh buffer medium was returned. Fe released ($R_{(Fe,n)}$) was calculated by the following equation:

$$R_{(Fe,n)}\ (\%) = \frac{20C_n + \sum_{i=1}^{n-1} C_i}{2 \times 1} \times 100\%$$

where C_n is the iron concentration tested in nth collection, C_i is the iron concentration in the ith collection. Unit of C_n and C_i are mg mL^{-1}.

In vitro MRI test

The *in vitro* MRI tests were conducted on a 3.0 T clinical MRI instrument (Philips). To test the *in vitro* longitudinal relaxation rate r_2, PEG/$Fe_2C@Fe_3O_4$ NPs at the iron concentration from 0.003 mM to 0.021 mM with the interval of 0.003 mM were dispersed in 1 mL of solution with pH 5.4 and 7.4 containing 1 wt% agarose gel respectively and placed in centrifuge tubes (1.5 mL). MR images were acquired using a T_2-weighted sequence with the following parameters: repetition time (T_R) = 500 ms; echo time (T_E) from 12.25 ms to 196 ms, with the interval of 12.25 ms; field of view (FOV) = 180 mm; slice thickness = 2 mm; NEX = 1.

Cell culture

4T1 cell line was obtained from the Zhejiang Provincial People's Hospital. All cell-culture-related reagents were purchased from Invitrogen. Cells were cultured in DMEM culture medium supplemented with 10% FBS and 1% penicillin/streptomycin at 37 °C under 5% CO_2 with 100% humidity.

The intracellular location of PEG/$Fe_2C@Fe_3O_4$ NPs in 4T1 cells

The as-prepared of PEG/$Fe_2C@Fe_3O_4$ NPs was labeled with fluorescein isothiocyanate (FITC) (λ_{ex} = 488 nm, λ_{em} = 517 nm) defined as PEG/$Fe_2C@Fe_3O_4$-FITC. 4T1 cells (5×10^4 cells per well) were seeded into a 24-well plate. When the cell confluence reached 80%, 300 μg mL^{-1} of PEG/$Fe_2C@Fe_3O_4$-FITC NPs were added into the culture medium and co-cultured with cells at 37 °C for 4 h. After that, 4T1 cells were counterstained with Lyso-Tracker red (λ_{ex} = 577 nm, λ_{em} = 590 nm) for 30 min and DAPI (λ_{ex} = 359 nm, λ_{em} = 461 nm) for 15 min. Finally, the cells were washed three times with PBS to remove the NPs that have not been endocytic. The images were taken by using a confocal microscope (Leica SP8).

Intracellular ROS burst detection

4T1 cells were plated at a density of 5×10^4 cells per well into a 24-well plate and were incubated for 12 h. Cells were loaded with 2,7-dichlorodihydrofluorescein diacetate (DCFH-DA, 10 μM) for 30 min and then washed with PBS for three times. Then, cells were treated by ART or PEG/$Fe_2C@Fe_3O_4$ NPs ([Fe] = 300 μg mL^{-1}) or PEG/$Fe_2C@Fe_3O_4$-ART NPs ([Fe] = 300 μg mL^{-1}). PEG/$Fe_2C@Fe_3O_4$-ART group has an equivalent ART dosage to the free ART group. The intensity of fluorescence was recorded every 15 min over a period of 9 h *via* excitation of 488 nm and emission at 525 nm by BioTek ELx800.

For the fluorescent microscopic examination, 4T1 cells with the cell density of 1×10^5 cells per well were plated onto coverslips in 12-well plates overnight. Then, cells were pre-stained with 10 μM DCFH-DA for 30 min and washed with PBS to remove the free DCFH-DA. Later, the cells were incubated with ART or PEG/$Fe_2C@Fe_3O_4$ NPs ([Fe] = 300 μg mL^{-1}) or PEG/$Fe_2C@Fe_3O_4$-ART NPs ([Fe] = 300 μg mL^{-1}) for 4 h before they were washed with PBS for three times. The images were acquired by a Leica SP8 confocal microscope with excitation at 488 nm and emission from 525 nm.

In vitro cytotoxicity assays

The *in vitro* cytotoxicity was evaluated by standard MTT assay. 4T1 cells were seeded into 96-well cell culture plates at 5×10^3 cells per well and incubated overnight at 37 °C under 5% CO_2. After that, cells were treated with various formulations of free ART, PEG/$Fe_2C@Fe_3O_4$, and PEG/$Fe_2C@Fe_3O_4$-ART at the same $Fe_2C@Fe_3O_4$ and ART concentrations. After further incubation for 24 h, the culture media were replaced by medium containing 0.5 mg mL^{-1} 3-[4,5-dimethylthiazol-2-yl-]-2,5-diphenyltetrazolium bromide (MTT). Finally, the MTT solution was replaced by 100 μL of dimethyl sulfoxide (DMSO) after co-incubation for 4 h. By using an ELISA reader (Tecan m200), cell proliferation was measured. Furthermore, after 4T1 cells were treated under the aforementioned conditions, cells were stained with calcein acetoxymethyl ester (calcein-AM, 2 μM, Yeason Biotech, China) and propidium iodide (PI, 4.5 μM, Yeason Biotech, China) to distinguish the live cells from dead cells through a fluorescence microscope (Nikon ECLIPSE Ti).

Assessment of apoptosis

Apoptotic status was determined by FITC-conjugated Annexin-V/PI assay kit (Sony) using flow cytometry following the manufacturer's instructions. Briefly, 5×10^4 per well 4T1 cells were seeded in 6-well plates for 12 h and treated with drugs for a further 24 h. The cells were rinsed with PBS and detached using EDTA-free trypsin. The detached cells were resuspended in 100 μL binding buffer containing FITC-conjugated Annexin-V/PI and incubated at RT for 15 min. The cells were diluted in 400 μL of buffer and analyzed by flow cytometry (NovoCyte 3130, USA). Apoptosis and necrosis were evaluated using PI *vs.* Annexin V plots. The cells stained with Annexin V only were classified as early apoptosis and the Annexin V and PI double-stained cells were classified as late apoptosis or necrosis.

Animal modal

All animal procedures were performed in accordance with the Guidelines for Care and Use of Laboratory Animals of Zhejiang

Chinese Medical University and experiments were approved by the Animal Ethics Committee of Zhejiang Chinese Medical University. 6 week female Balb/c mice, with an average weight of 17 g, were provided by the Shanghai Laboratory Animal Center, Shanghai, China. Mice were injected with 1×10^6 4T1 cells (0.1 mL cells in PBS) subcutaneously at the right axillary region.

Biodistribution studies

To qualitatively investigate the biodistribution of PEG/Fe_2-C@Fe_3O_4 NPs, 6 mice were assigned into two groups randomly. When the tumor volume reached to about 150 mm^3, mice were intravenously injected of PEG/$Fe_2C@Fe_3O_4$ NPs (10 mg_{Fe} kg^{-1}). In the magnetic targeting group, a magnet was located at the tumor site. Mice were sacrificed after heart perfusion at time point of 24 h with major organs (heart, liver, spleen, lung and kidneys) and tumors dissected, rinsed and weighted. The *in vivo* biodistribution of Fe element was then measured by ICP-AES and calculated as Fe percentage over administrated dose per gram of tissues.

In vivo tumor chemotherapy of PEG/$Fe_2C@Fe_3O_4$-ART

When the tumor volume reached to about 100 mm^3, 20 mice were randomly divided into 4 groups: (1) mice were intravenously injected of saline only as control; (2) mice were intravenously injected of saline with free ART; (3) mice were intravenously injected of saline with PEG/$Fe_2C@Fe_3O_4$-ART NPs; (4) mice were intravenously injected of saline with PEG/$Fe_2C@Fe_3O_4$-ART NPs as well as a magnet located at the tumor site. Both PEG/$Fe_2C@Fe_3O_4$-ART group and PEG/$Fe_2C@Fe_3O_4$-ART + magnet group have an equivalent ART dosage to the free ART group and have an equivalent particles dosage. All groups were injected once daily every three days in the period of 18 days with the dosage of 50 mg_{Fe} kg^{-1} and tumor volume was monitored 1 day post injection. Tumor volumes and body weight were monitored 1 day post injection during the treatment ($n = 5$). Tumor volume was calculated according to the formula of $(a \times b^2)/2$, where a and b are the long and short diameters of the tumor, respectively.

At given intervals of 19 days, mice from each group were euthanized and major visceral organs (heart, liver, spleen, lung, and kidney) and tumor were recovered, followed by fixing with 10% neutral buffered formalin. After the organs were embedded in paraffin and sectioned at 5 μm, hematoxylin and eosin (H&E) and TdT-mediated dUTP nick-end labeling (TUNEL) staining was performed. The slides were observed under optical microscope (Nikon ECLIPSE Ti).

Quantitative analysis of the ROS generation in tumors

At the 3rd day post injection, one mouse from each group was euthanized, and tumors were harvested from the necropsy. The tumor tissues were firstly embedded and frozen by an OCT (Jung, Tissue freezing medium, Leica). Cross sections of 10 μm thickness were cut using a cryomicrotome (Leica), staining with DCFH-DA, 10 μM for 30 min and mounted on the glass slides. The slides were then observed under a confocal microscope (Leica SP8, $\lambda_{ex} = 488$ nm; $\lambda_{em} = 525$ nm).

Statistical analysis

Quantitative data were expressed as mean ± s.d. One-way ANOVA statistical analysis was used to analyze differences between datum. Values with $p < 0.05$ were considered statistically significant (* means $p < 0.05$, ** means $p < 0.01$, *** means $p < 0.001$).

Author contributions

Fan Zhao: contributed equally to this work, carried out all experiments and performed the statistical analysis, contributed to discussion, writing – original draft. Jing Yu: contributed equally to this work, carried out all experiments and performed the statistical analysis, conceptualization, writing – review & editing. Weiliang Gao: participated in the animal studies and molecular biology experiments. Xue Yang: participated in the animal studies and molecular biology experiments. Liying Liang: participated in molecular biology experiments. Xiaolian Sun: supervision. Dan Su: supervision. Juan Li: supervision. Yao Ying: supervision. Wangchang Li: supervision. Liang Qiao: supervision. Jingwu Zheng: supervision. Wei Cai: supervision. Shenglei Che: conceptualization, supervision, writing – reviewing and editing. Xiaozhou Mou: conceptualization, supervision, writing – reviewing and editing.

Conflicts of interest

There are no conflicts to declare.

Acknowledgements

This work was supported in part by the National Natural Science Foundation of China (NSFC) (No. 52073258, 51602285, 81701821), Natural Science Foundation of Zhejiang Province (No. LY20E020017, LQ19H160016), Young Elite Scientist Sponsorship Program by CAST (No. 2017QNRC001), the Fundamental Research Funds for the Provincial Universities of Zhejiang (No. RF-A2019004), the Open Project Program of MOE Key Laboratory of Drug Quality Control and Pharmacovigilance (No. DQCP20/21MS02), and Foundation of Health Department of Zhejiang Province (No. 2018KY239, 2019RC010), and the Technological Program of Zhejiang Traditional Medicine (No. 2019ZB014).

References

1 Z. Shen, J. Song, B. C. Yung, Z. Zhou, A. Wu and X. Chen, Emerging strategies of cancer therapy based on ferroptosis, *Adv. Mater.*, 2018, **30**, 1704007.
2 Z. Tang, Y. Liu, M. He and W. Bu, Chemodynamic therapy: tumour microenvironment-mediated fenton and fenton-like reactions, *Angew. Chem., Int. Ed.*, 2019, **58**, 946–956.
3 C. Wu, S. Wang, J. Zhao, Y. Liu, Y. Zheng, Y. Luo, C. Ye, M. Huang and H. Chen, Biodegradable Fe(III)@WS_2-PVP nanocapsules for redox reaction and tme-enhanced

nanocatalytic, photothermal, and chemotherapy, *Adv. Funct. Mater.*, 2019, **29**, 1901722.

4 L. Wang, M. Huo, Y. Chen and J. Shi, Iron-engineered mesoporous silica nanocatalyst with biodegradable and catalytic framework for tumor-specific therapy, *Biomaterials*, 2018, **163**, 1–13.

5 M. Wu, Y. Ding and L. Li, Recent progress in the augmentation of reactive species with nanoplatforms for cancer therapy, *Nanoscale*, 2019, **11**, 19658–19683.

6 L.-S. Lin, J. Song, L. Song, K. Ke, Y. Liu, Z. Zhou, Z. Shen, J. Li, Z. Yang, W. Tang, G. Niu, H.-H. Yang and X. Chen, Simultaneous fenton-like ion delivery and glutathione depletion by MnO_2-based nanoagent to enhance chemodynamic therapy, *Angew. Chem., Int. Ed.*, 2018, **57**, 4902–4906.

7 Q. Chen, C. Liang, X. Sun, J. Chen, Z. Yang, H. Zhao, L. Feng and Z. Liu, H_2O_2-responsive liposomal nanoprobe for photoacoustic inflammation imaging and tumor theranostics via in vivo chromogenic assay, *Proc. Natl. Acad. Sci.*, 2017, **114**, 5343.

8 P. a. Ma, H. Xiao, C. Yu, J. Liu, Z. Cheng, H. Song, X. Zhang, C. Li, J. Wang, Z. Gu and J. Lin, Enhanced cisplatin chemotherapy by iron oxide nanocarrier-mediated generation of highly toxic reactive oxygen species, *Nano Lett.*, 2017, **17**, 928–937.

9 M. Huo, L. Wang, Y. Chen and J. Shi, Tumor-selective catalytic nanomedicine by nanocatalyst delivery, *Nat. Commun.*, 2017, **8**, 357.

10 L.-H. Fu, C. Qi, Y.-R. Hu, J. Lin and P. Huang, Glucose oxidase-instructed multimodal synergistic cancer therapy, *Adv. Mater.*, 2019, **31**, 1808325.

11 B. Wang, H. Zhang, J. An, Y. Zhang, L. Sun, Y. Jin, J. Shi, M. Li, H. Zhang and Z. Zhang, Sequential intercellular delivery nanosystem for enhancing ROS-Induced antitumor therapy, *Nano Lett.*, 2019, **19**, 3505–3518.

12 D. L. Klayman, Qinghaosu (Artemisinin): An antimalarial drug from china, *Science*, 1985, **228**, 1049–1055.

13 Y. Tu, Artemisinin—a gift from traditional chinese medicine to the world (Nobel Lecture), *Angew. Chem., Int. Ed.*, 2016, **55**, 10210–10226.

14 A. K. Das, Anticancer effect of antimalarial artemisinin compounds, *Ann. Med. Health Sci. Res.*, 2015, **5**, 93–102.

15 A. Bhaw-Luximon and D. Jhurry, Artemisinin and its derivatives in cancer therapy: status of progress, mechanism of action, and future perspectives, *Cancer Chemother. Pharmacol.*, 2017, **79**, 451–466.

16 Y. Chen, X. Lin, H. Park and R. Greever, Study of artemisinin nanocapsules as anticancer drug delivery systems, *Nanomedicine*, 2009, **5**, 316–322.

17 T. Efferth, A. Benakis, M. R. Romero, M. Tomicic, R. Rauh, D. Steinbach, R. Häfer, T. Stamminger, F. Oesch, B. Kaina and M. Marschall, Enhancement of cytotoxicity of artemisinins toward cancer cells by ferrous iron, *Free Radicals Biol. Med.*, 2004, **37**, 998–1009.

18 Y. K. Wong, C. Xu, K. A. Kalesh, Y. He, Q. Lin, W. S. F. Wong, H.-M. Shen and J. Wang, Artemisinin as an anticancer drug: recent advances in target profiling and mechanisms of action, *Med. Res. Rev.*, 2017, **37**, 1492–1517.

19 A. Shahbazfar, P. Zare, M. Ranjbaran, H. Tayefi-Nasrabadi, O. Fakhri, Y. Farshi, S. Shadi and A. Khoshkerdar, A survey on anticancer effects of artemisinin, iron, miconazole, and butyric acid on 5637 (bladder cancer) and 4T1 (Breast cancer) cell lines, *J. Cancer Res. Ther.*, 2014, **10**, 1057–1062.

20 J. Fu and Y. Zhu, Lysosomes activating chain reactions against cancer cells with a pH-switched prodrug/procatalyst co-delivery nanosystem, *J. Mater. Chem. B*, 2017, **5**, 996–1004.

21 H. Zhang, Q. Chen, X. Zhang, X. Zhu, J. Chen, H. Zhang, L. Hou and Z. Zhang, An intelligent and tumor-responsive Fe^{2+} donor and Fe^{2+}-dependent drugs cotransport system, *ACS Appl. Mater. Interfaces*, 2016, **8**, 33484–33498.

22 Y. Wang, Y. Han, Y. Yang, J. Yang, X. Guo, J. Zhang, L. Pan, G. Xia and B. Chen, Effect of interaction of magnetic nanoparticles of Fe_3O_4 and artesunate on apoptosis of K562 cells, *Int. J. Nanomed.*, 2011, **6**, 1185–1192.

23 Y. Ding, J. Wan, Z. Zhang, F. Wang, J. Guo and C. Wang, Localized Fe(II)-induced cytotoxic reactive oxygen species generating nanosystem for enhanced anticancer therapy, *ACS Appl. Mater. Interfaces*, 2018, **10**, 4439–4449.

24 H. Zhang, H. Zhang, X. Zhu, X. Zhang, Q. Chen, J. Chen, L. Hou and Z. Zhang, Visible-light-sensitive titanium dioxide nanoplatform for tumor-responsive Fe^{2+} liberating and artemisinin delivery, *Oncotarget*, 2017, **8**, 58738–58753.

25 N. Shterman, B. Kupfer and C. Moroz, Comparison of transferrin receptors, iron content and isoferritin profile in normal and malignant human breast cell lines, *Pathobiology*, 1991, **59**, 19–25.

26 J. Yu, F. Chen, W. Gao, Y. Ju, X. Chu, S. Che, F. Sheng and Y. Hou, Iron carbide nanoparticles: an innovative nanoplatform for biomedical applications, *Nanoscale Horiz.*, 2017, **2**, 81–88.

27 V. Davydov, A. Rakhmanina, I. Kireev, I. Alieva, O. Zhironkina, O. Strelkova, V. Dianova, T. D. Samani, K. Mireles, L. H. Yahia, R. Uzbekov, V. Agafonov and V. Khabashesku, Solid state synthesis of carbon-encapsulated iron carbide nanoparticles and their interaction with living cells, *J. Mater. Chem. B*, 2014, **2**, 4250–4261.

28 C. Giordano, A. Kraupner, S. C. Wimbush and M. Antonietti, Iron carbide: an ancient advanced material, *Small*, 2010, **6**, 1859–1862.

29 J. Yu, X. Chu and Y. Hou, Stimuli-responsive cancer therapy based on nanoparticles, *Chem. Commun.*, 2014, **50**, 11614–11630.

30 J. Yu, C. Yang, J. Li, Y. Ding, L. Zhang, M. Z. Yousaf, J. Lin, R. Pang, L. Wei, L. Xu, F. Sheng, C. Li, G. Li, L. Zhao and Y. Hou, Multifunctional Fe_5C_2 nanoparticles: a targeted theranostic platform for magnetic resonance imaging and photoacoustic tomography-guided photothermal therapy, *Adv. Mater.*, 2014, **26**, 4114–4120.

31 J. Yu, Y. Ju, L. Zhao, X. Chu, W. Yang, Y. Tian, F. Sheng, J. Lin, F. Liu, Y. Dong and Y. Hou, Multistimuli-regulated

photochemothermal cancer therapy remotely controlled via Fe_5C_2 nanoparticles, *ACS Nano*, 2016, **10**, 159–169.

32 Y. Ju, H. Zhang, J. Yu, S. Tong, N. Tian, Z. Wang, X. Wang, X. Su, X. Chu, J. Lin, Y. Ding, G. Li, F. Sheng and Y. Hou, Monodisperse Au–Fe_2C janus nanoparticles: an attractive multifunctional material for triple-modal imaging-guided tumor photothermal therapy, *ACS Nano*, 2017, **11**, 9239–9248.

33 J. Yu, F. Zhao, W. Gao, X. Yang, Y. Ju, L. Zhao, W. Guo, J. Xie, X.-j. Liang, X. Tao, J. Li, Y. Ying, W. Li, J. Zheng, L. Qiao, S. Xiong, X. Mou, S. Che and Y. Hou, Magnetic Reactive oxygen species nanoreactor for switchable magnetic resonance imaging guided cancer therapy based on pH-sensitive Fe_5C_2@Fe_3O_4 nanoparticles, *ACS Nano*, 2019, **13**, 10002–10014.

34 Z. Yang, T. Zhao, X. Huang, X. Chu, T. Tang, Y. Ju, Q. Wang, Y. Hou and S. Gao, Modulating the phases of iron carbide nanoparticles: from a perspective of interfering with the carbon penetration of Fe@Fe_3O_4 by selectively adsorbed halide ions, *Chem. Sci.*, 2017, **8**, 473–481.

35 C. Zhang, W. Bu, D. Ni, S. Zhang, Q. Li, Z. Yao, J. Zhang, H. Yao, Z. Wang and J. Shi, Synthesis of iron nanometallic glasses and their application in cancer therapy by a localized fenton reaction, *Angew. Chem., Int. Ed.*, 2016, **55**, 2101–2106.

36 X. Chen, H. Zhang, M. Zhang, P. Zhao, R. Song, T. Gong, Y. Liu, X. He, K. Zhao and W. Bu, Amorphous Fe-based nanoagents for self-enhanced chemodynamic therapy by re-establishing tumor acidosis, *Adv. Funct. Mater.*, 2019, **30**, 1908365.

37 A. Lawal, R. A. Umar, M. G. Abubakar, U. Z. Faruk and U. Wali, FTIR and UV-Visible spectrophotometeric analyses of artemisinin and its derivatives, *J. Pharm. Biomed. Sci.*, 2012, **24**, 6–14.

38 M. A. Kohanski, D. J. Dwyer, B. Hayete, C. A. Lawrence and J. J. Collins, A common mechanism of cellular death induced by bactericidal antibiotics, *Cell*, 2007, **130**, 797–810.

39 N. C. Yip, I. S. Fombon, P. Liu, S. Brown, V. Kannappan, A. L. Armesilla, B. Xu, J. Cassidy, J. L. Darling and W. Wang, Disulfiram modulated ROS-MAPK and NFκB pathways and targeted breast cancer cells with cancer stem cell-like properties, *Br. J. Cancer*, 2011, **104**, 1564.

40 P. Liu, S. Brown, P. Channathodiyil, V. Kannappan, A. L. Armesilla, J. L. Darling and W. Wang, Cytotoxic effect of disulfiram/copper on human glioblastoma cell lines and ALDH-positive cancer-stem-like cells, *Br. J. Cancer*, 2013, **108**, 9940–9942.